Journal of
Materials Chemistry C

ROYAL SOCIETY OF CHEMISTRY

PAPER

View Article Online
View Journal | View Issue

Cite this: *J. Mater. Chem. C*, 2023, **11**, 8214

A low-symmetry monothiatruxene-based hole transport material for planar n–i–p perovskite solar cells with 18.9% efficiency†

Ellie Tanaka, ‡[a] Gyu Min Kim, §[b] Michał R. Maciejczyk,¶[a] Ayumi Ishii, ‖[b] Gary S. Nichol, [a] Tsutomu Miyasaka *[b] and Neil Robertson *[a]

Received 10th January 2023,
Accepted 17th March 2023

DOI: 10.1039/d3tc00119a

rsc.li/materials-c

Hole transport materials (HTMs) based on truxene cores have emerged as promising candidates in recent years. They are noted by properties such as higher hole mobility and higher glass transition temperature than the 2,2′,7,7′-tetrakis (*N*,*N*-di-*p*-methoxyphenamine)-9,9′-spirobiflourene (spiro-MeOTAD), as well as good hydrophobicity and energy alignment. Truxene derivatives have been studied for application in transistors, OLEDs, lasers, supercapacitors, *etc.*, however, there are only a few studies on their use as HTMs in perovskite solar cells (PSCs). In this study, we synthesised a novel small organic molecule HTM with a monothiatruxene (TrxS) core, namely TrxS-2MeOTAD, and characterised its basic properties and ability as an HTM in n–i–p planar PSCs. The TrxS-2MeOTAD showed suitable electrochemical, optical, structural and thermal properties for an HTM, such as a relatively high glass transition temperature (145 °C) and stable amorphous nature when deposited as films. The PSCs using TrxS-2MeOTAD achieved 18.9% power conversion efficiency (PCE) compared to the reference spiro-MeOTAD at 19.3% PCE. The unencapsulated TrxS-2MeOTAD devices showed better operational stability than spiro-MeOTAD, with a 1.5 times longer lifetime under constant AM1.5G illumination. Our results suggest that small molecules based on the TrxS core can be a promising direction for the development of alternative HTMs.

10th Anniversary Statement

I have been heavily involved with *Journal of Materials Chemistry C* as an Associate Editor for nearly nine years, hence for nearly all of its existence as a separate journal. Back in 2014, I was delighted to be offered the opportunity to join the editorial team and to contribute what I can to the journal's development. In addition to the overall quality of JMCC, the attraction for me has always been the breadth across so many types of organic and inorganic materials for applications including optical, electronic and magnetic topics. I don't think any other journal would have given me the chance for such a complete overview of functional materials. I will complete my time as Associate Editor later this year, but am looking forward to continuing my involvement with JMCC as an author and reader, and am sure it will continue to go from strength to strength over its second decade. Neil Robertson, January 2023.

Introduction

In recent years, perovskite solar cells (PSCs) have attracted tremendous interest as a readily-processed and efficient emerging solar technology.[1–6] Organic small molecules such as 2,2′,7,7′-tetrakis[*n*,*n*-di(4-methoxyphenyl)amino]-9,9′-spirobifl-uorene (spiro-MeOTAD or spiro-OMeTAD) have been the classic hole transport materials (HTMs) in PSCs owing to the wide range of possible core/substituent

---

[a] *School of Chemistry, University of Edinburgh, Kings Buildings, Edinburgh, EH9 3FJ, UK. E-mail: neil.robertson@ed.ac.uk*

[b] *Graduate School of Engineering, Toin University of Yokohama, 1614 Kuroganecho, Aoba, Yokohama, Kanagawa, 225-8503, Japan*

† Electronic supplementary information (ESI) available: Solar cell fabrication and characterization; synthesis of compounds; single crystal X-ray diffraction; fabrication and characterisation of SCLC devices; UV/Vis absorption and photoluminescence; computational calculations; cyclic voltammetry; powder X-ray diffraction; scanning electron microscopy. CCDC 2235428 and 2235429. For ESI and crystallographic data in CIF or other electronic format see DOI: https://doi.org/10.1039/d3tc00119a

‡ Current address: Science & Innovation Center, Mitsubishi Chemical Corporation, 1000 Kamoshidacho, Aoba, Yokohama, Kanagawa, 227-8502, Japan.

§ Current address: Faculty of Food Biotechnology and Chemical Engineering, Hankyong National University, Anseong, Gyeonggi-Do, 17579, Republic of Korea.

¶ Current address: Cambridge Display Technology Limited, Unit 12 Cardinal Park, Cardinal Way, Godmanchester, Cambridgeshare, PE29 2XG, UK.

‖ Current address: Faculty of Life and Environmental Sciences, Teikyo University of Science, 2525 Yatsusawa, Uenohara, Yamanashi, 409-0193, Japan.

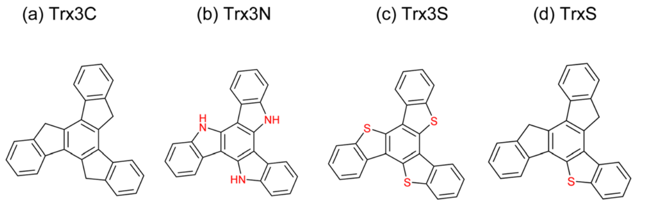

Fig. 1 Molecular representation of (a) truxene (Trx3C), (b) triazatruxene (Trx3N), (c) trithiatruxene (Trx3S) and (d) monothiatruxene (TrxS). There have been no prior studies on (d) as the basis for a hole transport material in solar cells.

designs, solubility and amorphous nature when deposited as thin films.[7–11] Despite the relatively high performance *ca.* 20% that has been consistently achieved across many labs using spiro-MeOTAD as the HTM in PSCs,[12–14] there remain some limitations: (1) the short lifetime of the final PSC due to the hygroscopic additives *i.e.* lithium bis(trifluoromethanesulfonyl)imide (LiTFSI) and *tert*-butyl pyridine (*t*BP) in the HTM, and (2) the costly synthesis and purification of the spiro-MeOTAD. When designing a new organic small molecule HTM, the selection of the core structure will greatly influence the properties and cost of the final HTM. Such examples include the spiro[fluorene-9,90-xanthene] (SFX) core and phenothiazine core, where the materials showed power conversion efficiencies (PCEs) comparable to spiro-MeOTAD with greatly reduced cost.[15–18]

HTMs based on truxene cores (Fig. 1) have emerged as promising candidates in the last few years. They are noted by properties such as higher hole mobility and higher glass transition temperature than the spiro-MeOTAD as well as good hydrophobicity and energy alignment.[19] Truxene derivatives have so far been studied for application in transistors, OLEDs, lasers, supercapacitors, *etc.*, however, there are only a few studies of their use as HTMs in PSCs. Huang *et al.* demonstrated a truxene (Trx3C) based HTM and achieved 18.6% in an inverted p–i–n PSC.[20] Rakstys *et al.* studied a number of triazatruxene (Trx3N) based HTMs to achieve 18–19% PCE in mesoporous n–i–p PSCs.[21,22] Meanwhile, Maciejczyk *et al.* reported a new monothiatruxene core (TrxS),[23] which displayed merged properties of the Trx3C and Trx3S, whereby the low symmetry may lead to a greater potential to form uniform, amorphous films. The oxidised form of TrxS (TrxSO2) has been demonstrated to display exceptional properties in blue organic light-emitting materials,[24] however this remains the only application sought for this class of materials. In this study, we therefore explore the potential of TrxS-based materials as HTMs in PSCs by synthesising a simple methoxydiphenylamine (MeODPA) substituted derivative (TrxS-2MeOTAD). The design of the molecule was chosen based on computational DFT calculations. The newly synthesised HTM shows good solubility, high glass transition temperature, sufficient hole mobility and stability. Planar n–i–p PSCs using the new molecule achieved 18.9% PCE—comparable with the reference spiro-MeOTAD at 19.3% PCE. The unencapsulated solar cell using TrxS-2MeOTAD showed better operation stability than spiro-MeOTAD, with a 1.5 times longer lifetime under constant AM1.5 illumination.

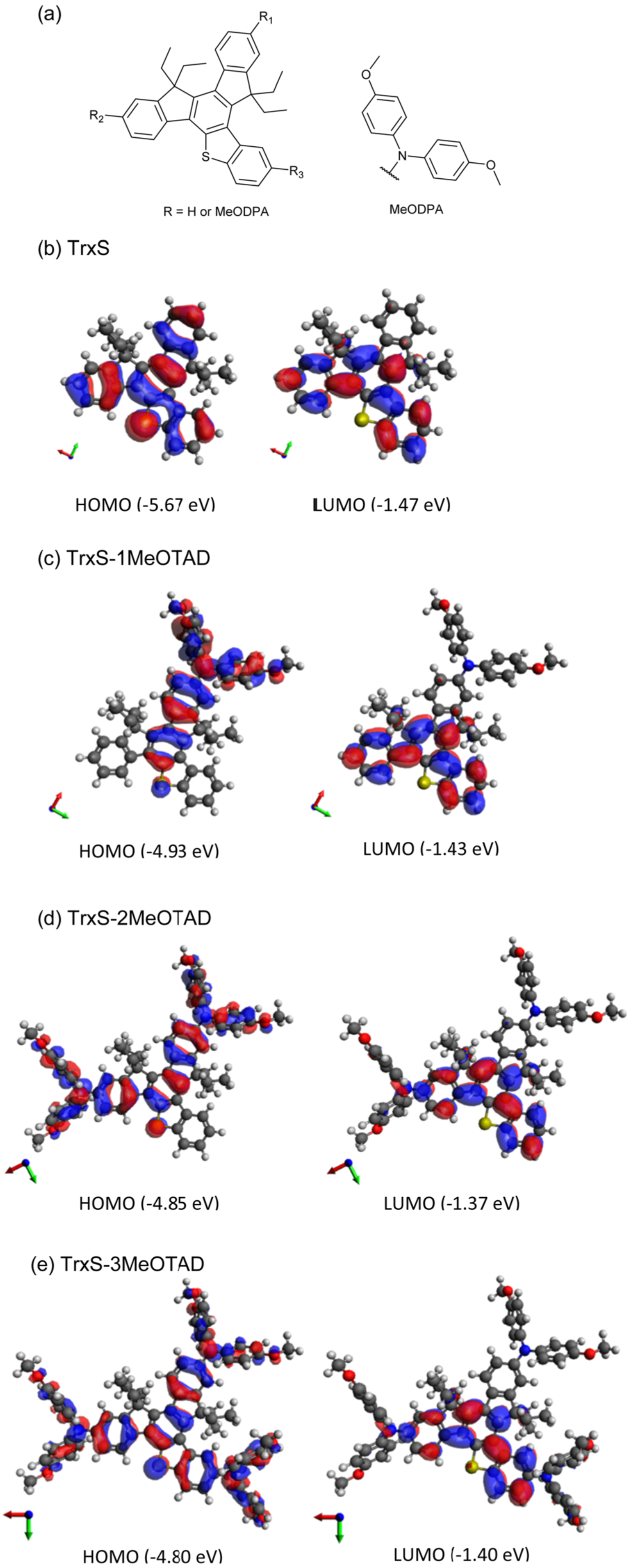

Fig. 2 (a) Molecular representation of the TrxS core and MeODPA substituent. Variations considered in the calculations were: R1 = R2 = R3 = H (TrxS); R1 = MeODPA and R2 = R3 = H (TrxS-1MeOTAD); R1 = R2 = MeODPA and R3 = H (TrxS-2MeOTAD) and R1 = R2 = R3 = MeODPA (TrxS-3MeOTAD). HOMO and LUMO of (b) TrxS, (c) TrxS-1MeOTAD, (d) TrxS-2MeOTAD and (e) TrxS-3MeOTAD in dichloromethane, calculated by B3LYP 6-311G(d).

Table 1 HOMO and LUMO levels calculated for TrxS-MeOTAD with varying number of MeODPA moieties

	HOMO[a] (G)/eV	LUMO[a] (G)/eV	HOMO[b] (S)/eV	LUMO[b] (S)/eV	E_g[c] (G)/eV	E_g[d] (S)/eV
TrxS	−5.52	−1.35	−5.67	−1.47	4.17	4.20
TrxS-1MeOTAD	−4.78	−1.24	−4.93	−1.43	3.54	3.50
TrxS-2MeOTAD	−4.65	−1.14	−4.85	−1.37	3.51	3.48
TrxS-3MeOTAD	−4.56	−1.13	−4.80	−1.40	3.43	3.40

[a] HOMO and LUMO levels calculated for the compound in gas state. [b] HOMO and LUMO levels calculated for the compound in the liquid state with DCM as solvent. [c] HOMO–LUMO gap derived from LUMO (G)–HOMO (G). [d] HOMO–LUMO gap derived from LUMO (S)–HOMO (S).

Results and discussion

Materials and synthesis

Design of the molecule. Prior to the synthesis of the new compound, the HOMO and LUMO levels were estimated by DFT calculation using B3LYP 6-311G(d) basis set. The HOMO energy alignment with the perovskite in the solar cell is important to realise efficient charge transport. The energy levels were calculated in the gas phase and in the solvent field (dichloromethane – DCM) to allow better comparison with the solution spectroscopy and electrochemical results. Monothiatruxene (TrxS) with diethyl substitution was used as the core, where the R_1–R_3 positions were varied from substitution by zero to three methoxydiphenylamine (MeODPA) moieties (Fig. 2). Hereafter, we will denote these TrxS derivatives as TrxS-*x*MeOTAD, where *x* is the number of the MeODPA substituents on the TrxS core. For example, TrxS-1MeOTAD indicates a TrxS derivative with R_1 = MeODPA R_2 = R_3 = H. TrxS-2MeOTAD indicates a TrxS derivative with R_1 = R_2 = MeODPA and R_3 = H. The calculated energy levels are summarised in Table 1.

Table 1 shows the rise in HOMO level when the number of MeODPA moieties increases. The wide bandgaps derived from the liquid-state calculations suggest the compounds to be

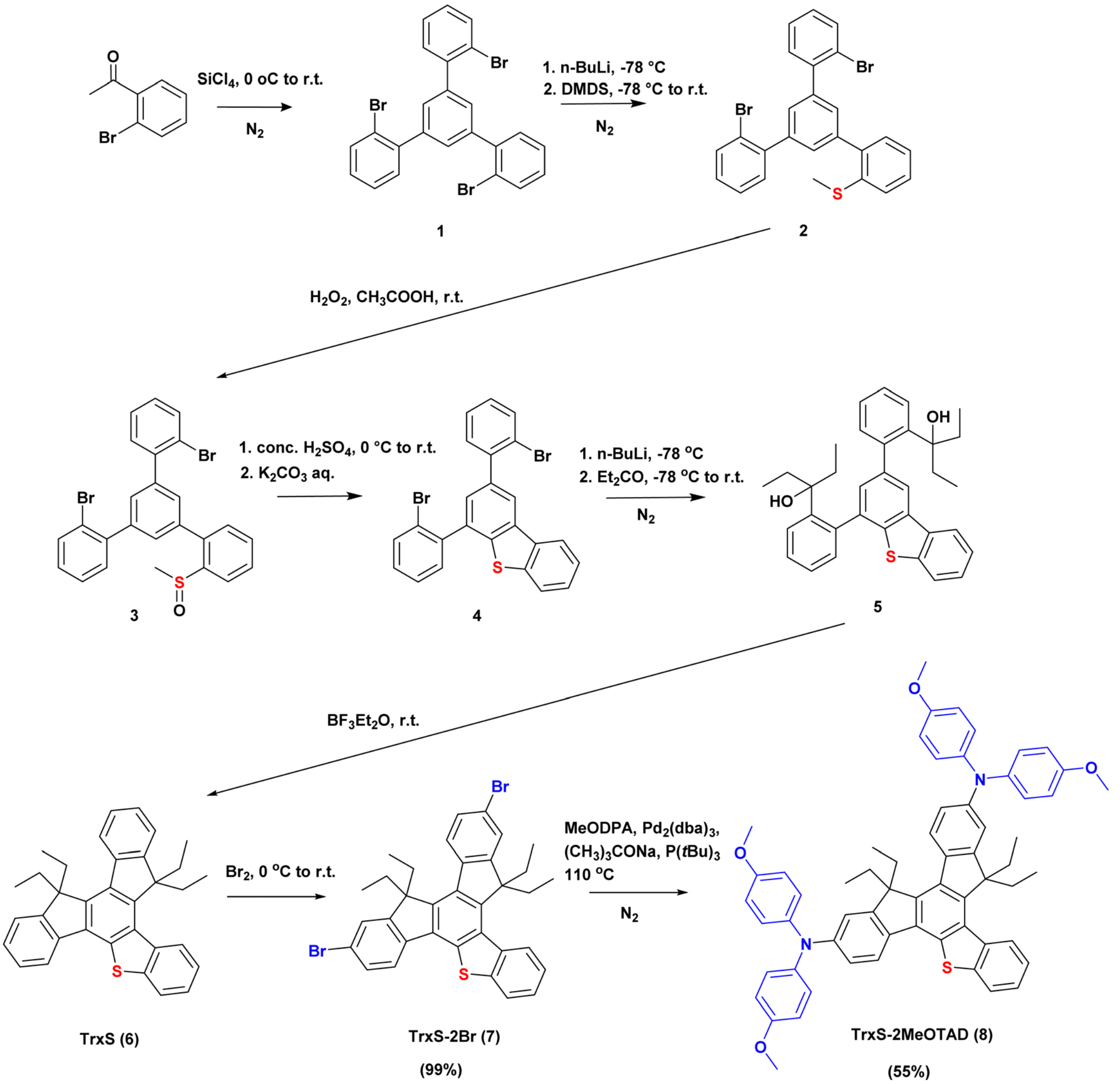

Fig. 3 Synthesis scheme of TrxS-2MeOTAD. Full details are given in the Experimental section. The percentage in brackets is the synthesis yield.

optically transparent in the visible, which is advantageous for an HTM since it will not absorb any of the light that should be harvested by the perovskite. The HOMO level of the HTM should be assessed based on the valence band edge energy of the lead-halide perovskite, typically in the range of *ca.* −5.9 eV to −5.3 eV ($CsPbI_3$: −5.3 eV;[25] $MAPbI_3$: −5.4 eV;[26] $(FAPbI_3)_{0.95}(MAPbBr_3)_{0.05}$: −5.5 eV;[27] $CsPbI_2Br$: −5.8 eV;[28] $CsPbBr_3$: −5.9 eV).[25] The HOMO of the HTM should be higher than the valence band energy of the perovskite, therefore TrxS with predicted HOMO (L) = −5.67 eV would possibly work for some of the perovskite materials studied but probably not with the commonest perovskite formulas such as $MAPbI_3$. The energy levels in general are seen to shift to lower values when the solvent field is applied. This can be explained by the enhanced stability of the more polarizable state by DCM solvent. The energy levels are expected to lower further in the solid state. The >0.7 eV upward shift in HOMO level from TrxS to *x*MeOTAD (*x* from 1 to 3) can be explained by the extended HOMO over the MeODPA moiety once substituted. HOMO/LUMO locations for TrxS, TrxS-2MeOTAD and TrxS-3MeOTAD are shown in Fig. 2. When MeODPA is substituted, the HOMO evenly distributes over the MeODPA, bridged by the TrxS core, while the LUMO is concentrated on the TrxS core.

TrxS-2MeOTAD with two MeODPA substituents was selected as the target molecule in this study, based on the predicted energy levels and predicted simplicity of the synthesis. The overall synthesis scheme is described in Fig. 3.

Synthesis of TrxS-2MeOTAD

The synthesis of TrxS is based on the reports by Maciejczyk *et al.*[23,24] TrxS-2Br and TrxS-2MeOTAD were synthesised for the first time in this study. The bromination of TrxS resulted in an excellent yield of 99% and further purification of TrxS-2Br was not required before the synthesis of TrxS-2MeOTAD. The final TrxS-2MeOTAD was synthesised by Buchwald–Hartwig amination of the TrxS-2Br with 4,4′-dimethoxydiphenylamine. Details of the syntheses are provided in the ESI.†

Electrochemical analysis

The electrochemical properties of TrxS-2MeOTAD were investigated by cyclic voltammetry (Fig. 4(a)) in DCM solution, with ferrocene used as internal standard.[29] Two oxidation peaks with a difference of 90 mV were detected as presented in the square wave voltammogram in Fig. 4(b). For the first oxidation peak the proportionality of $I_{1/2}$ (mean of I_{pa} and I_{pc}) against the square-root of the scan rate ($\nu^{0.5}$) (Fig. 4(c)); the negligible difference between I_{pa} and I_{pc}; the scan rate independence of $E_{1/2}$; and ΔE_p values around 60 mV (Fig. 4(d)) indicate good chemical and electrochemical reversibility, important for good stability of the HTM in the PV cell, and rapid electron transfer, important for high hole mobility.

The HOMO level of TrxS-2MeOTAD is similar to the value reported for spiro-MeOTAD (−5.22 eV *vs.* −5.14 eV)[15,30] and is in a suitable range for most common perovskites for PSCs. However, the experimental HOMO value turned out to be lower

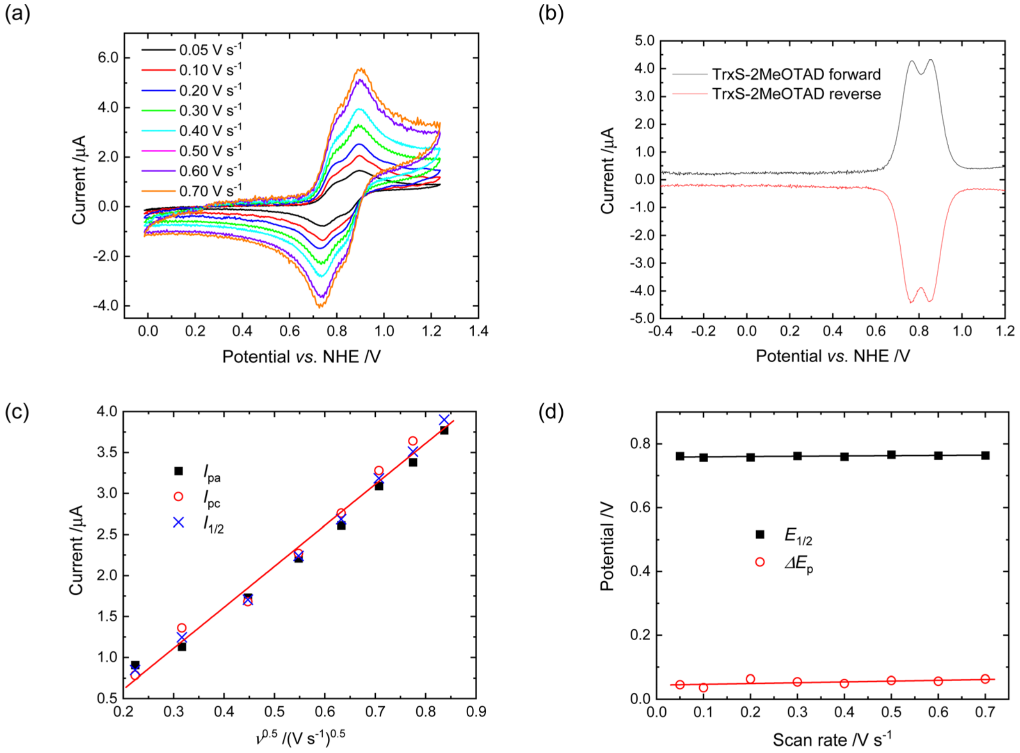

Fig. 4 (a) Cyclic voltammogram of TrxS-2MeOTAD at different scan rates ranging from 0.05 V s^{-1} to 0.70 V s^{-1}. (b) Square wave voltammogram of TrxS-2MeOTAD at a scan rate of 0.05 V s^{-1}. (c) I_{pa}, I_{pc} and $I_{1/2}$ *versus* square-root of the scan rate $\nu^{0.5}$ derived from (a); R^2 = 0.992 for the linear fitting of $I_{1/2}$. (d) $E_{1/2}$ and ΔE_p *versus* scan rate, derived from (a).

Table 2 Experimental values of electrochemical and optical properties of TrxS-2MeOTAD. Literature data for spiro-MeOTAD are shown as a reference

HTM	$\lambda_{max}{}^{a}$/nm ($\varepsilon/10^5$ M^{-1} cm^{-1})	$\lambda_{em}{}^{b}$/nm	$E_{ox}{}^{c}$/V	$E_{HOMO}{}^{d}$/eV	$E_{LUMO}{}^{e}$/eV	$E_g{}^{f}$/eV
TrxS-2MeOTAD	360[a] (7.37)	440	0.761 (0.764)	−5.22 (−5.22)	−2.20	3.02
Spiro-MeOTAD[g]	385	424	—	−5.14	−2.16	2.98

[a] Absorption peak from UV/Vis absorption (molar extinction coefficient in parenthesis). [b] Emission peak detected by excitation at λ_{max}. [c] Half-wave potential ($E_{1/2}$) from CV (peak potential from SWV in parenthesis), referenced to NHE. [d] Calculated from E_{HOMO} [eV] = $-E_{OX}$ [V] − 4.456 (value from SWV in parenthesis).[30] [e] Calculated from $E_{LUMO} = E_{HOMO} + E_g$. [f] Optical gap derived from UV/Vis absorption and PL measurements. [g] Data from the literature.[15]

than the calculated value by 0.37 eV, which may be too low for some perovskites and in such cases the HOMO level of TrxS-3MeOTAD may be in a more suitable range.

Optical properties

The absorption and emission properties of the TrxS-2MeOTAD are shown in Fig. S1(a) (ESI†). The absorption peak (λ_{max}) and emission peak (λ_{em}) do not shift from solution to film, which is an indication of the amorphous nature for the film. Compared to the solution, the TrxS-2MeOTAD film shows a tail at lower energies for both absorption and emission, which could be interpreted as some intermolecular interaction. The film is colourless, which is confirmed by the absence of any absorption in the visible. The experimental values for the electrochemical and optical data are summarised in Table 2.

Thermal properties

The thermal properties were assessed by thermo gravimetric-differential thermal analysis (TG-DTA) (Fig. 5(a)) and differential scanning calorimetry (DSC) (Fig. 5(b)). The properties are summarised in Table S1 (ESI†). TrxS-2MeOTAD displays an endothermic peak at 223 °C (or 221 °C from the DSC), accompanied by a small endothermic peak at 260 °C (or 261 °C from the DSC). With both points having no weight losses, the first prominent peak at 223 °C is apparently the melting point (T_m), while the small peak could be related to some polymorphic change of the material. The TG curve shows one step of weight loss from 333 °C (0.5% weight loss at *ca.* 400 °C) with an exothermic peak at 460 °C, assignable to decomposition. 45% of the initial weight was lost during this step until the end of

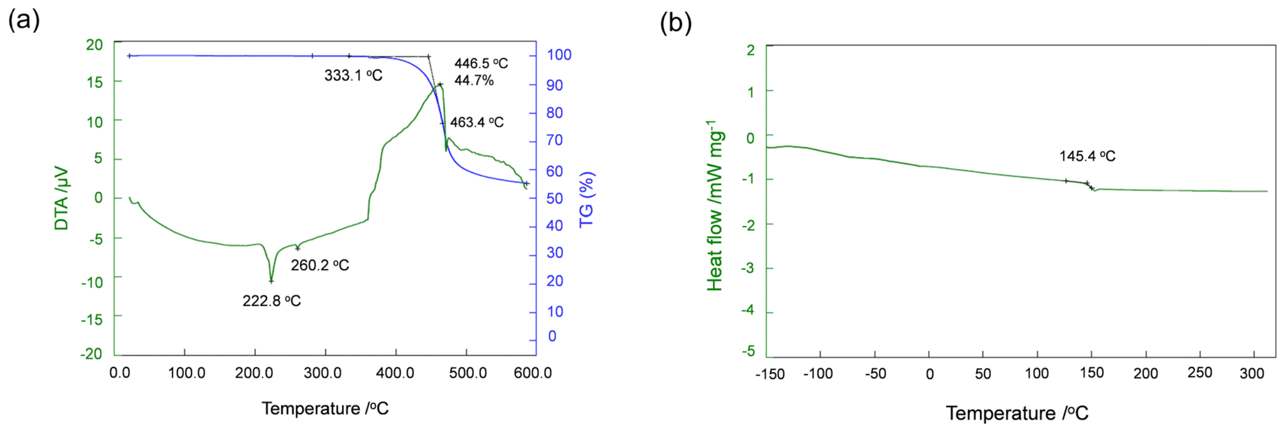

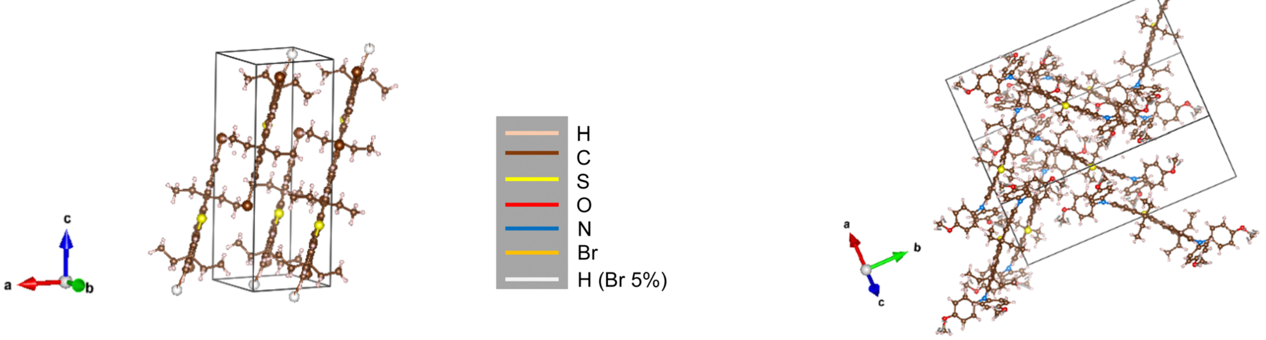

(c) TrxS-2Br

(d) TrxS-2MeOTAD

Fig. 5 (a) TG-DTA curves of TrxS-2MeOTAD. The blue curve indicates the TG, with a decomposition onset at 333 °C. (b) Second heating profile of the DSC to determine the glass temperature (T_g). (c) The crystal structures of TrxS-2Br (CCDC 2235428†) and (d) that of TrxS-2MeOTAD (CCDC 2235429†) from the SXRD analysis. The images were created by the Vesta software.[37] White spheres are marked in the TrxS-2Br image because the recrystallised crystal was found to contain *ca.* 5% of tribrominated TrxS-3Br. This, we believe, does not affect the interpretation of the SXRD analysis.

the measurement at 590 °C. In Fig. S2 (ESI†), a shift of the baseline before the melting point suggests that TrxS-2MeOTAD has a glass transition temperature (T_g) at 145 °C. This is higher than that of spiro-MeOTAD at 122 °C, indicating that TrxS-2MeOTAD has relatively high stability in its rigid glassy state. No cold crystallisation was observed, in contrast to the case for some organic small molecules including spiro-MeOTAD.[15] To further explore the thermal stability we compared SEM images of the spin-coated TrxS-2MeOTAD before heating, after heating for 10 minutes at 135 °C, and after heating for 10 minutes at 155 °C (*i.e.* 10 °C below and above T_g respectively) (Fig. S8, ESI†). We observe very limited change in the images after heating, with a similar amorphous appearance at higher temperature. Overall, the results indicate that TrxS-2MeOTAD has high thermal stability as an organic small molecule, making it compatible for an HTM in PSCs.

Structural properties of TrxS-2MeOTAD

The crystal structures of TrxS-2Br and TrxS-2MeOTAD were solved from single crystals as shown in Fig. 5(c and d). Full crystal parameters are listed in Table S2 (ESI†). TrxS-2Br was found to crystallise in triclinic $P\bar{1}$ space group, whereas TrxS-2MeOTAD was found to crystallise in monoclinic $P2_1/c$ space group. The TrxS-2Br molecules displayed π–π stacking, with interactions of 3.557 Å. The crystal packing of TrxS-2MeOTAD is more complicated, with the molecules stacking in a zigzag form. This apparently comes from the twisted MeODPA moiety, with a dihedral angle of 123.3°. π–π interactions of 3.68 Å were observed, which explains the high T_g and melting point. The X-ray powder diffraction (PXRD) patterns of TrxS-2MeOTAD in powder form and as a spin-coated film on microscope glass slide along with simulated PXRD pattern from the SXRD analysis are shown in Fig. S3 (ESI†). TrxS-2MeOTAD powder showed preferred orientation towards the (100) facet, with one prominent peak at $2\theta = 5.4°$ followed by several other small peaks. The spin-coated film from chlorobenzene did not show any peaks, indicating that the TrxS-2MeOTAD film is amorphous.

Hole mobility of TrxS-2MeOTAD

The space-charge limited current (SCLC) was measured for hole-only devices to assess the hole mobility of TrxS-2MeOTAD. A hole only device with the structure ⟨ITO/PEDOT:PSS/HTM/Au⟩ (ITO = indium-doped tin oxide, PEDOT:PSS = poly(3,4-ethylenedioxythiophene polystyrene sulfonate) was tested and compared with a similar device using spiro-MeOTAD as the HTM. Both HTMs were doped with the optimised ratio of dopants for each. The *J*–*V* curves that were used to derive the hole mobility are shown in Fig. 6(a). The slope of $J^{0.5}$ *vs.* V (denoted as $C^{0.5}$) was used to derive the hole mobility μ from the following relation:

$$J\left[\text{mA cm}^{-2}\right] = \left(\frac{9}{8}\varepsilon\varepsilon_0\mu\cdot\frac{1}{d^3}\right)V^2 = CV^2, \qquad (1)$$

where ε is the dielectric constant which is assumed as 3 (a typical number for most organic semiconductors),[31] ε_0 is the permittivity of free space (8.854×10^{-12} [F m^{-1}]), μ is the hole mobility [cm^2 V^{-1} s^{-1}], d is the thickness of the HTM layer [nm], and V is the applied voltage [V]. The slopes in the linear regions in Fig. 6(a) were derived as 11.82 for spiro-MeOTAD and 10.27 for TrxS-2MeOTAD. This results in a hole mobility of 1.28×10^{-3} [cm^2 V^{-1} s^{-1}] for spiro-MeOTAD and 3.53×10^{-4} [cm^2 V^{-1} s^{-1}] for TrxS-2MeOTAD. Thus, for these doped materials, the mobility of TrxS-MeOTAD was measured as ∼3 times lower than spiro-MeOTAD, but is in a sufficient range to achieve high performance in PSCs.

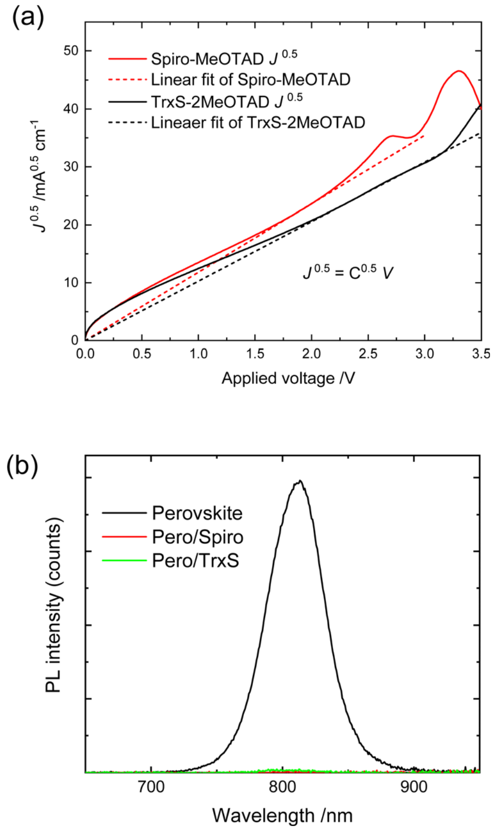

Fig. 6 (a) $J^{0.5}$–V curves used to derive the hole mobility from SCLC measurements. (b) Steady-state photoluminescence spectra of spiro-MeOTAD/perovskite and TrxS-2MeOTAD/perovskite films.

Photoluminescence quenching

The steady-state and time-resolved PL were measured for a device structure of ⟨Glass/Perovskite/HTM⟩ for TrxS-2MeOTAD and spiro-MeOTAD. The steady-state PL is shown in Fig. 6(b) and the time-resolved PL decay curves are shown in Fig. S4 (ESI†). While the EQE of the ⟨glass/perovskite⟩ derived from the steady-state PL was 1.1%, the EQE of ⟨Glass/Perovskite/TrxS-2MeOTAD⟩ and ⟨Glass/Perovskite/spiro-MeOTAD⟩ were both approximately zero. Both steady-state and time-resolved measurements confirm that the TrxS-2MeOTAD sufficiently quenches the PL of the perovskite by efficient hole extraction.

Photovoltaic performance

The PSCs were fabricated in dry atmosphere, *i.e.*, with normal oxygen content and humidity below 2%. The devices had a

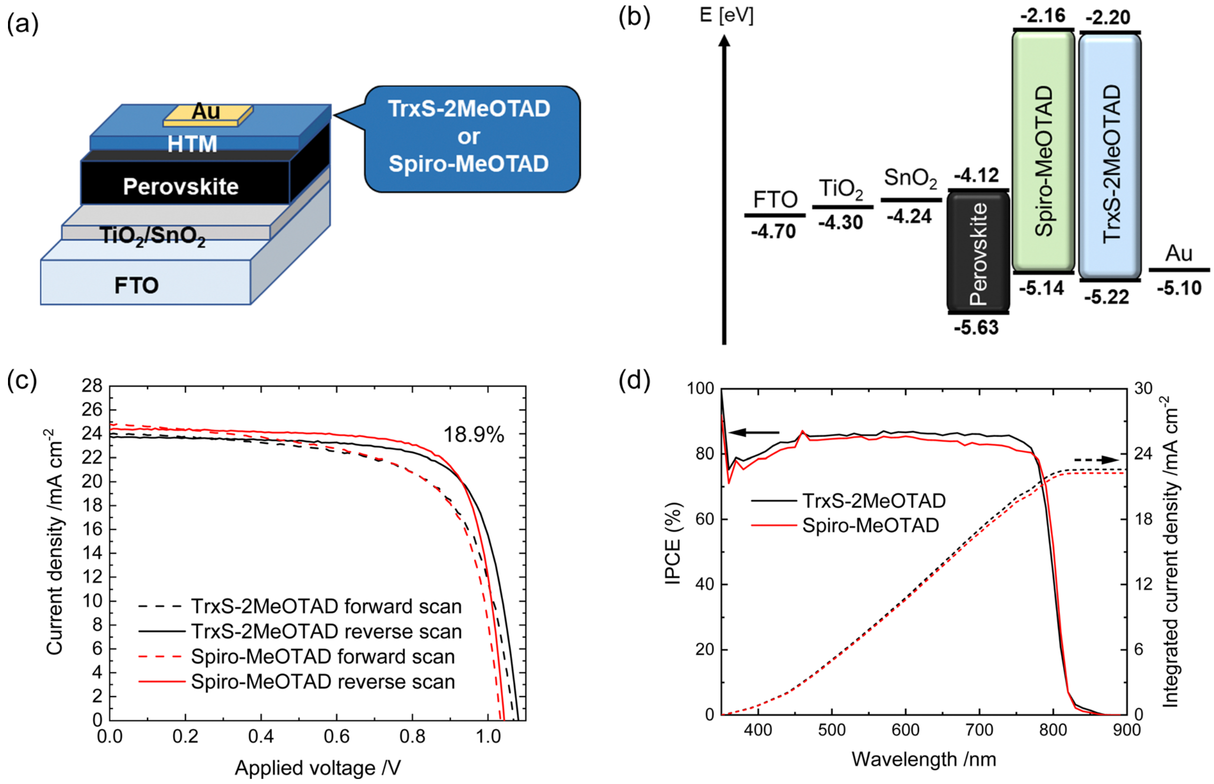

Fig. 7 (a) The PSC device structure employed in this study. (b) The corresponding energy level diagram. The values for FTO, TiO_2, SnO_2 and Au were taken from the literature. (c) *J–V* curves of the best TrxS-2MeOTAD PSC and spiro-MeOTAD PSC fabricated in this study. (d) The corresponding IPCE curves.

general structure of fluorine-doped tin oxide (FTO)/TiO_2/SnO_2/Perovskite/HTM/Au, where the perovskite was a triple-cation $Cs_{0.04}(FA_{0.83}MA_{0.17})_{0.96}Pb(I_{0.95}Br_{0.05})_3$ (FA = formamidinium, MA = methylammonium) as shown in Fig. 7(a and b).[32] The HTM and dopant (LiTFSI and *t*BP) concentration in the spin-coating solution were independently optimised for TrxS-2MeOTAD (Fig. S5 and S6, ESI†). The performance of the optimised TrxS-2MeOTAD PSC (40 mM HTM, HTM/LiTFSI/*t*BP = 1 : 0.55 : 3.3 (mol/mol)) and spiro-MeOTAD PSC (60 mM HTM, HTM/LiTFSI/*t*BP = 1 : 0.55 : 3.3 (mol/mol)) are summarised in Table 3. The corresponding *J–V* curves are shown in Fig. 7(c) along with the incident photon-to-current efficiency (IPCE) spectra (Fig. 7(d)). The best TrxS-2MeOTAD PSC exhibited 18.9% PCE, nearing spiro-MeOTAD with 19.3% PCE. Interestingly, the J_{SC}, V_{OC}, ff and hysteresis of the TrxS-2MeOTAD were all very similar to the spiro-MeOTAD PSC. It is seen from Fig. 7(c) that the J_{SC} is slightly higher for the spiro-MeOTAD and the V_{OC} is slightly higher for the TrxS-2MeOTAD.

Table 3 PSCs with the best performance for TrxS-2MeOTAD and spiro-MeOTAD

HTM	Scan	J_{SC}/mA cm^{-2}	V_{OC}/V	ff	PCE/%
TrxS-2MeOTAD	Forward	24.0	1.07	0.66	16.9
	Reverse	23.8	1.08	0.73	18.9
Spiro-MeOTAD	Forward	24.8	1.03	0.66	16.8
	Reverse	24.3	1.04	0.76	19.3

The IPCE spectra in Fig. 7(d) indicate that the light-to-electricity conversion is also similar for the whole spectral absorption range. The integrated J_{SC} derived from the IPCE spectra was 22.6 mA cm^{-2} for TrxS-2MeOTAD and 22.3 mA cm^{-2} for spiro-MeOTAD, which are sufficiently close to the values obtained by the *J–V* measurements. Overall, the results confirm that the TrxS-2MeOTAD HTM works efficiently in n–i–p PSCs.

Structural properties of the TrxS-2MeOTAD PSCs

Fig. S7(a) (ESI†) shows the PXRD patterns of the optimised PSCs incorporating TrxS-2MeOTAD or spiro-MeOTAD as the HTM. Both patterns only show peaks associated with the perovskite or FTO substrate, which indicates that the HTM layers are amorphous in the PSC. This is consistent with the PXRD pattern of the TrxS-2MeOTAD film coated on a microscope glass slide (Fig. S3, ESI†).

SEM images of the cross-section of the PSCs employing TrxS-2MeOTAD and spiro-MeOTAD are shown in Fig. S7(b and c) (ESI†). A uniform layer and smooth interfaces with the perovskite and gold are observed for both HTMs. No grain boundaries are seen in either of the samples, indicating again that the TrxS-2MeOTAD forms amorphous layers similar to spiro-MeOTAD.

Stability of the PSCs

The operational stability of the PSC is equally important to the performance itself. Fig. 8 compares the performance of

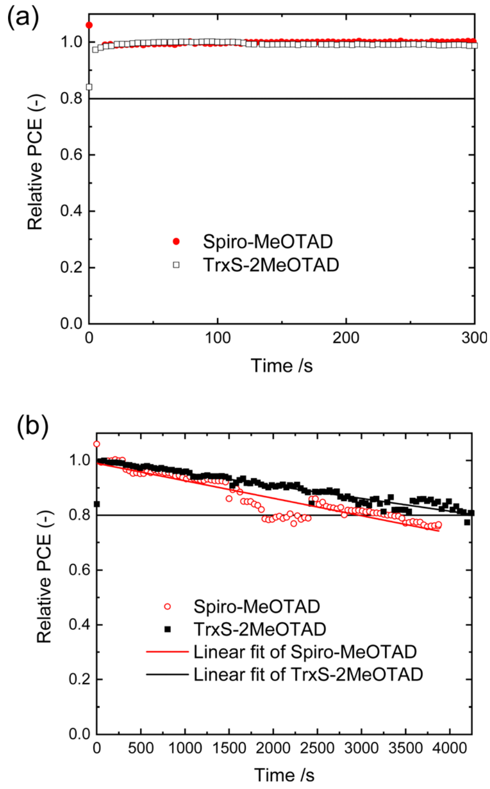

Fig. 8 Operational stability of TrxS-2MeOTAD compared with spiro-MeOTAD (ISOS-L-1). The cells were held at a constant voltage, at the initial maximum power point and the current density was recorded under constant illumination at 1 sun until the current (and calculated efficiency) dropped to 80% of the initial value. (a) From t = 0 s to t = 300 s. (b) From t = 0 to t = 4000 s.

unencapsulated PSCs using TrxS-2MeOTAD and spiro-MeOTAD as HTM, tracked under constant illumination at 1 sun in ambient air for an hour (stability assessment protocol ISOS-L-1).[33] The device was held at a constant voltage at the initial maximum power point and the photocurrent was constantly recorded. The PCE was derived by multiplying the recorded current density with the fixed voltage. Fig. 8(a) shows that both spiro-MeOTAD and TrxS-2MeOTAD PSCs maintained a constant power output for the first 300 s. The PCE at this point was taken as the ''initial'' PCE in Fig. 8(b). Fig. 8(b) indicates that the TrxS-2MeOTAD PSC has a longer lifetime than the spiro-MeOTAD PSC. The linear fitting was $y = 1 - 6.79 \times 10^{-5}x$ for spiro-MeOTAD and $y = 1 - 4.63 \times 10^{-5}x$ for TrxS-2MeOTAD, where y is the relative PCE (%) and x is the time [s]. The fitting for TrxS-MeOTAD results in an operational lifetime of T_{80} = 4320 s (time until 20% PCE drop), which is *ca.* 1.5 times longer compared to the spiro-MeOTAD PSC at T_{80} = 2946 s. The higher operational stability of TrxS-2MeOTAD could be attributed to the properties of the HTM itself, or to the lower amount of LiTFSI contained in the corresponding PSC (as demonstrated by the lower concentration of the HTM in the spin-coating solution and the thinner film observed by SEM). Further insights on the photo/thermo/moisture stability could be gained if the devices were measured in a designated environment for each specific condition. Overall, The TrxS-MeOTAD has been demonstrated to display relatively high stability in addition to the excellent performance in PSCs.

Conclusions

In summary, a novel organic small molecule TrxS-2MeOTAD with a monothiatruxene core was successfully synthesised and its basic properties were investigated. The electrochemical, optical, structural and thermal properties were found to be suitable for an HTM in n–i–p PSCs. The TrxS-2MeOTAD showed higher glass transition temperature compared to the spiro-MeOTAD, with a stable amorphous nature when deposited as films. The TrxS-2MeOTAD displayed similar photovoltaic performance to spiro-MeOTAD in n–i–p planar PSCs when doped with common dopants LiTFSI and *t*BP. Hole mobility and PL decay analyses confirmed that the material works as an efficient hole extractor and transporter. Finally, the operational stability of the PSC using TrxS-2MeOTAD was demonstrated to be higher than that using spiro-MeOTAD, which we assume is due to the better thermal stability and lower level of doping required with the new HTM. Interestingly, using spiro-MeOTAD, we see a partial recovery of PCE at 2500 s before the degradation resumes. Such partial recovery has been observed before, albeit associated with a rest period for the cell.[34–36] These results all together indicate that TrxS based HTMs can be a promising direction for the development of alternative HTMs. More widely, the study of HTMs based on a low-symmetry core may prove a convenient route to amorphous films of good thermal stability. In addition, the close crystal packing and high orientation observed in the crystalline form provokes interest in testing these materials as HTMs in inverted planar PSCs.

Conflicts of interest

There are no conflicts to declare.

Acknowledgements

ET acknowledges JASSO for a PhD studentship. The authors acknowledge the Royal Society of Chemistry for a Researcher Mobility Grant towards collaborative research. TM would like to thank Mitsubishi Chemical Corporation for the TG-DTA and DSC measurements. Some crystal data were collected remotely at beam line I-19 of Diamond Light Source (award CY22240). We thank Jiayi Zhao and Xuerui Yi for carrying out the heated-sample SEM experiments.

References

1 A. Kojima, K. Teshima, Y. Shirai and T. Miyasaka, *J. Am. Chem. Soc.*, 2009, **131**, 6050–6051.
2 M. M. Lee, J. Teuscher, T. Miyasaka, T. N. Murakami and H. J. Snaith, *Science*, 2012, **338**, 643–647.

3 H.-S. Kim, C.-R. Lee, J.-H. Im, K.-B. Lee, T. Moehl, A. Marchioro, S.-J. Moon, R. Humphry-Baker, J.-H. Yum, J. E. Moser, M. Grätzel and N.-G. Park, *Sci. Rep.*, 2012, **2**, 591.

4 M. A. Green and A. Ho-Baillie, *ACS Energy Lett.*, 2017, **2**, 822–830.

5 A. K. Jena, A. Kulkarni and T. Miyasaka, *Chem. Rev.*, 2019, **119**, 3036–3103.

6 T. Wu, Z. Qin, Y. Wang, Y. Wu, W. Chen, S. Zhang, M. Cai, S. Dai, J. Zhang, J. Liu, Z. Zhou, X. Liu, H. Segawa, H. Tan, Q. Tang, J. Fang, Y. Li, L. Ding, Z. Ning, Y. Qi, Y. Zhang and L. Han, *Nano-Micro Lett.*, 2021, **13**, 1–18.

7 H. D. Pham, L. Xianqiang, W. Li, S. Manzhos, A. K. K. Kyaw and P. Sonar, *Energy Environ. Sci.*, 2019, **12**, 1177–1209.

8 L. Nakka, Y. Cheng, A. G. Aberle and F. Lin, *Adv. Energy Sustainability Res.*, 2022, **3**, 2200045.

9 H. D. Pham, Z. Wu, L. K. Ono, S. Manzhos, K. Feron, N. Motta, Y. Qi and P. Sonar, *Adv. Electron. Mater.*, 2017, **3**, 1700139.

10 H. D. Pham, S. M. Jain, M. Li, S. Manzhos, K. Feron, S. Pitchaimuthu, Z. Liu, N. Motta, H. Wang, J. R. Durrant and P. Sonar, *J. Mater. Chem. A*, 2019, **7**, 5315–5323.

11 H. D. Pham, S. M. Jain, M. Li, Z. K. Wang, S. Manzhos, K. Feron, S. Pitchaimuthu, Z. Liu, N. Motta, J. R. Durrant and P. Sonar, *Adv. Electron. Mater.*, 2020, **6**, 1900884.

12 F. M. Rombach, S. A. Haque and T. J. Macdonald, *Energy Environ. Sci.*, 2021, **14**, 5161–5190.

13 Z. Hawash, L. K. Ono and Y. Qi, *Adv. Mater. Interfaces*, 2018, **5**, 1700623.

14 S. Gangala and R. Misra, *J. Mater. Chem. A*, 2018, **6**, 18750–18765.

15 M. Maciejczyk, A. Ivaturi and N. Robertson, *J. Mater. Chem. A*, 2016, **4**, 4855–4863.

16 B. Xu, D. Bi, Y. Hua, P. Liu, M. Cheng, M. Grätzel, L. Kloo, A. Hagfeldt and L. Sun, *Energy Environ. Sci.*, 2016, **9**, 873–877.

17 J. Salunke, X. Guo, Z. Lin, J. R. Vale, N. R. Candeias, M. Nyman, S. Dahlström, R. Österbacka, A. Priimagi, J. Chang and P. Vivo, *ACS Appl. Energy Mater.*, 2019, **2**, 3021–3027.

18 M. R. Maciejczyk, R. Chen, A. Brown, N. Zheng and N. Robertson, *J. Mater. Chem. C*, 2019, **7**, 8593–8598.

19 K. H. Lin, A. Prlj and C. Corminboeuf, *J. Phys. Chem. C*, 2017, **121**, 21729–21739.

20 C. Huang, W. Fu, C. Z. Li, Z. Zhang, W. Qiu, M. Shi, P. Heremans, A. K. Y. Jen and H. Chen, *J. Am. Chem. Soc.*, 2016, **138**, 2528–2531.

21 K. Rakstys, A. Abate, M. I. Dar, P. Gao, V. Jankauskas, G. Jacopin, E. Kamarauskas, S. Kazim, S. Ahmad, M. Grätzel and M. K. Nazeeruddin, *J. Am. Chem. Soc.*, 2015, **137**, 16172–16178.

22 K. Rakstys, S. Paek, P. Gao, P. Gratia, T. Marszalek, G. Grancini, K. T. Cho, K. Genevicius, V. Jankauskas, W. Pisula and M. K. Nazeeruddin, *J. Mater. Chem. A*, 2017, **5**, 7811–7815.

23 M. R. Maciejczyk, J. A. G. Williams, N. Robertson and M. Pietraszkiewicz, *RSC Adv.*, 2017, **7**, 49532–49535.

24 M. R. Maciejczyk, S. Zhang, G. J. Hedley, N. Robertson, I. D. W. Samuel and M. Pietraszkiewicz, *Adv. Funct. Mater.*, 2018, **1807572**, 1–13.

25 C. Liu, M. Hu, X. Zhou, J. Wu, L. Zhang, W. Kong, X. Li, X. Zhao, S. Dai, B. Xu and C. Cheng, *NPG Asia Mater.*, 2018, **10**, 552–561.

26 J. Liu, Y. Wu, C. Qin, X. Yang, T. Yasuda, A. Islam, K. Zhang, W. Peng, W. Chen and L. Han, *Energy Environ. Sci.*, 2014, **7**, 2963–2967.

27 N. J. Jeon, H. Na, E. H. Jung, T. Y. Yang, Y. G. Lee, G. Kim, H. W. Shin, S. Il Seok, J. Lee and J. Seo, *Nat. Energy*, 2018, **3**, 682–689.

28 Z. Guo, A. K. Jena, I. Takei, G. M. Kim, M. A. Kamarudin, Y. Sanehira, A. Ishii, Y. Numata, S. Hayase and T. Miyasaka, *J. Am. Chem. Soc.*, 2020, **142**, 9725–9734.

29 R. R. Gagne, C. A. Koval and G. C. Lisensky, *Inorg. Chem.*, 1980, **19**, 2854–2855.

30 C. M. Cardona, W. Li, A. E. Kaifer, D. Stockdale and G. C. Bazan, *Adv. Mater.*, 2011, **23**, 2367–2371.

31 Y. Li, R. G. Clevenger, L. Jin, K. V. Kilway and Z. Peng, *J. Mater. Chem. C*, 2014, **2**, 7180.

32 S. S. Mali, J. V. Patil, H. Arandiyan and C. K. Hong, *J. Mater. Chem. A*, 2019, **7**, 17516–17528.

33 M. V. Khenkin, E. A. Katz, A. Abate, G. Bardizza, J. J. Berry, C. Brabec, F. Brunetti, V. Bulović, Q. Burlingame, A. Di Carlo, R. Cheacharoen, Y.-B. Cheng, A. Colsmann, S. Cros, K. Domanski, M. Dusza, C. J. Fell, S. R. Forrest, Y. Galagan, D. Di Girolamo, M. Grätzel, A. Hagfeldt, E. von Hauff, H. Hoppe, J. Kettle, H. Köbler, M. S. Leite, S. (Frank) Liu, Y.-L. Loo, J. M. Luther, C. Q. Ma, M. Madsen, M. Manceau, M. Matheron, M. McGehee, R. Meitzner, M. K. Nazeeruddin, A. F. Nogueira, Ç. Odabaşı, A. Osherov, N.-G. Park, M. O. Reese, F. De Rossi, M. Saliba, U. S. Schubert, H. J. Snaith, S. D. Stranks, W. Tress, P. A. Troshin, V. Turkovic, S. Veenstra, I. Visoly-Fisher, A. Walsh, T. Watson, H. Xie, R. Yıldırım, S. M. Zakeeruddin, K. Zhu and M. Lira-Cantu, *Nat. Energy*, 2020, **5**, 35–49.

34 G. Wenson, H. Thakkar, H. Tsai, J. Stein, R. Singh and W. Nie, *J. Mater. Chem. A*, 2022, **10**, 13519–13526.

35 S. W. Lee, S. Kim, S. Bae, K. Cho, T. Chung, L. E. Mundt, S. Lee, S. Park, H. Park, M. C. Schubert, S. W. Glunz, Y. Ko, Y. Jun, Y. Kang, H. S. Lee and D. Kim, *Sci. Rep.*, 2016, **6**, 38150.

36 J. Carolus, T. Merckx, Z. Purohit, B. Tripathi, H. G. Boyen, T. Aernouts, W. De Ceuninck, B. Conings and M. Daenen, *Sol. RRL*, 2019, **3**, 1900226.

37 K. Momma and F. Izumi, *J. Appl. Crystallogr.*, 2011, **44**, 1272–1276.